



High-zeta-potential accelerates interface charge transfer in lithium anodes via MXene-graphdiyne heterojunction layers

Lu Sun^a, Meifeng Li^a, Jianan Gu^{b,*}, Yingfeng Li^b, Jinzhang Liu^a, Yan Li^{a,*}, Meicheng Li^{b,*}

^a School of Materials Science and Engineering, Beihang University, 100191, Beijing, China

^b State Key Laboratory of Alternate Electrical Power System with Renewable Energy Sources, School of New Energy, North China Electric Power University, 100096, Beijing, China

ARTICLE INFO

Keywords:

MXene-graphdiyne
High-zeta-potential
Interface charge transfer
Dendrite-free
Lithium anodes

ABSTRACT

Lithium (Li) metal anodes are a crucial part of lithium-based batteries and are highly regarded as a top contender for achieving high-energy-density lithium batteries. However, the development of dendrites and other related issues have significantly impeded their practical applications. Here, we fabricated a MXene (Ti₃C₂T_x)-graphdiyne heterostructure layer anode with high-zeta-potential (−90 mV) using an electrostatic self-assembly method. The high-zeta-potential can accelerate the interface charge transfer in the lithium deposition process, facilitating the uniform Li nucleation on the surface of anodes. Theoretical simulations further reveal that the high-zeta-potential can not only reduce the lithium ion concentration gradient but also homogenize the electric field in the anodes. Besides, based on first-principles computation, the adsorption energy of lithium atoms on MXene-graphdiyne heterostructure is −3.4 eV. As a result, a low overpotential of 12.4 mV has been achieved by MXene-graphdiyne layers at 0.05 mA cm^{−2}. Additionally, MXene-graphdiyne-Li anodes display an ultralong cycle life upto 1400 h and good rate capability upto 8 mA cm^{−2} in symmetric cells. Full cells consisting of MXene-graphdiyne-Li anodes and LiFeO₄ cathodes also show stable cyclic properties (300 cycles at 5C).

1. Introduction

The demand for lithium-based batteries has significantly increased with the rapid development of portable electronics, electric vehicles, and electric storage stations. As an essential component of lithium-based batteries, the lithium (Li) metal anode has emerged as a promising candidate for high-energy-density lithium batteries [1–7]. However, metallic Li anodes suffer deteriorative dendrite-related issues, which lead to low Coulombic efficiency and severe volume expansion [8–13]. Even more concerning, rigid Li dendrites can penetrate the membrane during repeated discharge-charge cycles, causing short circuits in the battery and creating potential safety hazards. These issues significantly impede the practical application of Li anodes [14–18].

The Sand's time model suggests that the formation of Li dendrites involves two main stages: nucleation and growth. These stages are influenced by the local current density of the electrodes, the transfer of lithium ions and electrons, and the initial concentration gradient of the lithium ion flux [19]. Several strategies have been adopted to prevent the formation of Li dendrites and promote uniform Li deposition. These approaches include adjusting the structure of electrodes [9,20],

regulating the components of the solid electrolyte interphase (SEI) film [21–23], and controlling the nucleation of Li metal [24]. For instance, using a three-dimensional electrode structure has proven effective in reducing local current density as well as increasing Li plating-stripping capacities. Liang and his co-workers were able to achieve high Li capacities of up to 30 mAh cm^{−2} through the 3D covalently cross-linked MXene scaffold [25]. Besides, the application of *in-situ* or *ex-situ* artificial SEI films has been demonstrated to promote the fast transfer of Li ions and electrons, realizing high-rate property [26,27]. Although 3D hosts and artificial SEI films are effective strategies to regulate the growth stage of lithium, they tend to overlook the importance of the nucleation stage of lithium growth. Alternatively, controlling the initial deposition stage of Li can obtain homogeneous nucleation and leading to controllable Li growth. For instance, approaches that leverage lithiophilicity, such as lithiophilic sites [28], metal solutions [29], and chemical bonding, have been shown to significantly lower the barrier for lithium nucleation and promote uniform Li nucleation. The Sand's time model indicates that the charge transfer of Li⁺ and electrons plays a crucial role in Li nucleation. Therefore, accelerating the interface charge transfer can be an alternative approach to obtaining uniform Li

* Corresponding authors.

E-mail addresses: gujianan@ncepu.edu.cn (J. Gu), liyan@buaa.edu.cn (Y. Li), mcli@ncepu.edu.cn (M. Li).

<https://doi.org/10.1016/j.cej.2023.144014>

Received 10 April 2023; Received in revised form 24 May 2023; Accepted 6 June 2023

Available online 8 June 2023

1385-8947/© 2023 Elsevier B.V. All rights reserved.

nucleation and growth.

Here, $Ti_3C_2T_x$ -graphdiyne heterostructure layers (MXene-graphdiyne) were fabricated using a simple electrostatic self-assembly method to accelerate the interface charge transfer during the lithium deposition process (Fig. 1). The MXene-graphdiyne heterostructure layers have a high-zeta-potential of -90 mV, which facilitates the fast and uniform nucleation of Li on their surfaces by overcoming the diffusion-limited current. Furthermore, COMSOL Multiphysics simulations have shown that the high-zeta-potential of MXene-graphdiyne heterostructure layers can highly reduce the lithium ion concentration gradient and homogenize the electric field in the anodes. Density functional theory (DFT) calculations have also demonstrated that the adsorption energy of Li atoms on the MXene-graphdiyne heterostructure is 3.4 eV. As a result, a low overpotential of 12.4 mV has been exhibited by MXene-graphdiyne layers at 0.05 mA cm^{-2} . Besides, MXene-graphdiyne-Li anodes display an ultralong cycle life upto 1400 h and good rate capability upto 8 mA cm^{-2} in symmetric cells. When combined with $LiFeO_4$ cathodes, full cells consisting of MXene-graphdiyne-Li anodes also display stable cycling properties for 300 cycles at 5C.

2. Results and discussion

The synthetic route of MXene-graphdiyne is schematically illustrated in Fig. 2a. First, MXene layers and graphdiyne nanosheets were obtained by exfoliating from the etched Ti_3AlC_2 material and bulk graphdiyne using the methods previously reported, respectively [30–32]. Subsequently, the graphdiyne nanosheets were modified with a cationic polymer, poly(diallyldimethylammonium chloride) (PDDA), to provide a surface positive charge. The positively charged graphdiyne nanosheets (38.7 mV) were then electrostatically attached to the negatively charged MXene layers (-14.9 mV), which was confirmed by the zeta-potential measurement (Figure S1). The as-prepared MXene-PDDA-graphdiyne samples exhibited a positive surface charge due to the existence of excess PDDA (Figure S2), which may lower the conductivity of MXene-graphdiyne and hinder its electrochemical performance. Thus, acetone solvent was adopted to remove the PDDA. After the removal of PDDA, the heterostructure was stabilized by $\pi-\pi^*$ and Ti-C bonds and formed a 2D MXene-graphdiyne nanoarchitecture, in which the content of graphdiyne is $\sim 50\%$. (Fig. 2a) (for more details, see the Supporting Information).

The microstructure and morphology of the MXene-graphdiyne layers was characterized by transmission electron microscopy (TEM) and high-

resolution TEM measurement (HRTEM). In Figure S3, the layer-by-layer structure with a lateral size of ~ 2 μm is observed, where graphdiyne nanoflakes are covered by wider MXene layers. The TEM image shows the close contact between MXene and graphdiyne nanosheets. The HRTEM image of the MXene-graphdiyne layers (Fig. 2b) indicates the coexistence of $Ti_3C_2T_x$ (1101) facet with the lattice spacing of 0.26 nm and graphdiyne with the fringe spacing of 0.36 nm [33,34]. Furthermore, selected area electron diffraction (Figure S4) confirms the presence of both $Ti_3C_2T_x$ and graphdiyne, indicating the successful synthesis of the MXene-graphdiyne heterogeneous interface and the tight integration of the two materials. Element mapping of MXene-graphdiyne layers in Figure S5 demonstrates a homogeneous element distribution of Ti, C, O, and F.

Raman measurements provide additional evidence for the incorporation of graphdiyne with MXene. As shown in Fig. 2c, MXene-graphdiyne exhibits both Raman signals arising from the MXene in the range of 150 to 750 cm^{-1} [30], as well as peaks at 1396 cm^{-1} (D band), 1582 cm^{-1} (G band), 1926 cm^{-1} and 2182 cm^{-1} (vibration of conjugated diyne linkage) corresponding to the graphdiyne species [35]. The Fourier transform infrared spectroscopy analysis (Figure S6) confirms the successful incorporation of both MXene and graphdiyne components in the synthesized material. Specifically, the absorption peaks at $1490-1700$ cm^{-1} and $2191-2450$ cm^{-1} can be attributed to the skeletal vibration of the benzene ring and the stretching vibration of the alkynyl group, respectively, which correspond to the $C=C$ (sp^2 benzene ring) and $C\equiv C$ (sp^3 alkynyl) chemical bonds (Figure S6). Furthermore, the interaction between MXene and graphdiyne were elucidated by X-ray photoelectron spectroscopy (XPS). Fig. 2d compares C1s spectra of MXene-graphdiyne, MXene and graphdiyne, respectively. For the MXene-graphdiyne, the C1s XPS spectrum exhibits signals from both MXene and graphdiyne as well as another two additional peaks (at 290.0 and 281.8 eV) are not observed in MXene or graphdiyne. The weak peak at 290 eV should attributed to the $\pi-\pi^*$ transition bond, verifying the interaction between graphdiyne and MXene [36]. The newly emerged peak at 281.8 eV in MXene-graphdiyne may originate from the Ti-C bond formation between surface Ti atoms from MXene and sp -hybridized C atoms in graphdiyne, as the acetylene bond ratio (1:1) is much lower than that in graphdiyne (1:2) [37]. Moreover, the binding energy of Ti2p (Figure S7) in MXene-graphdiyne has shifted towards lower binding energy compared to that of MXene. This shift implies the presence of a chemical interaction as well as electron transfer from graphdiyne to MXene [32]. To obtain a better understanding of the

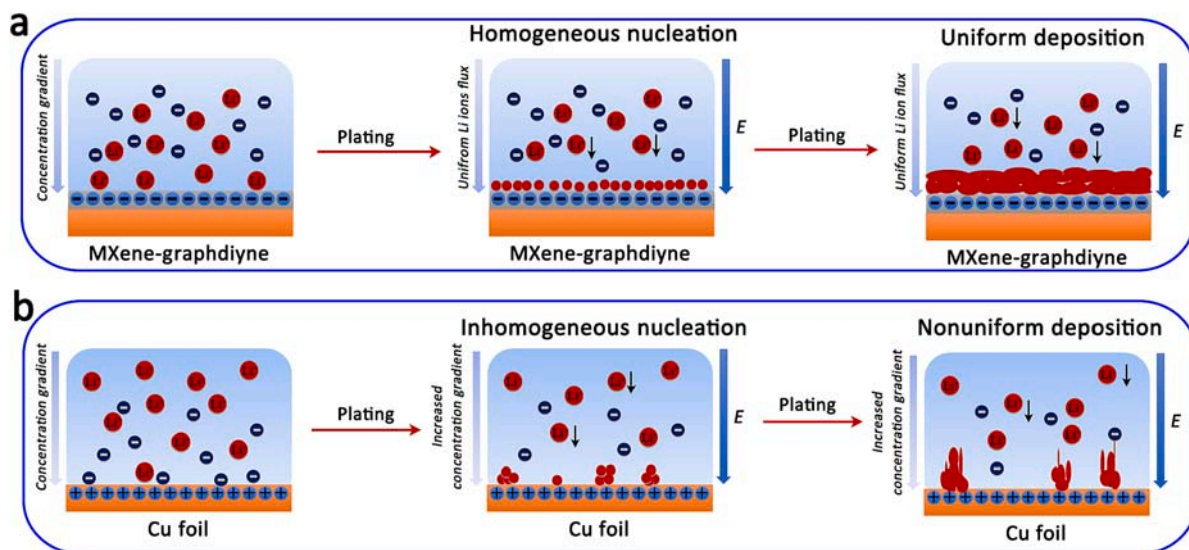


Fig. 1. Illustration of Li plating behavior of a) MXene-graphdiyne and b) pure Cu foil. The MXene-graphdiyne layers with high-zeta-potential accelerate the interface charge transfer, leading to uniform Li deposition.

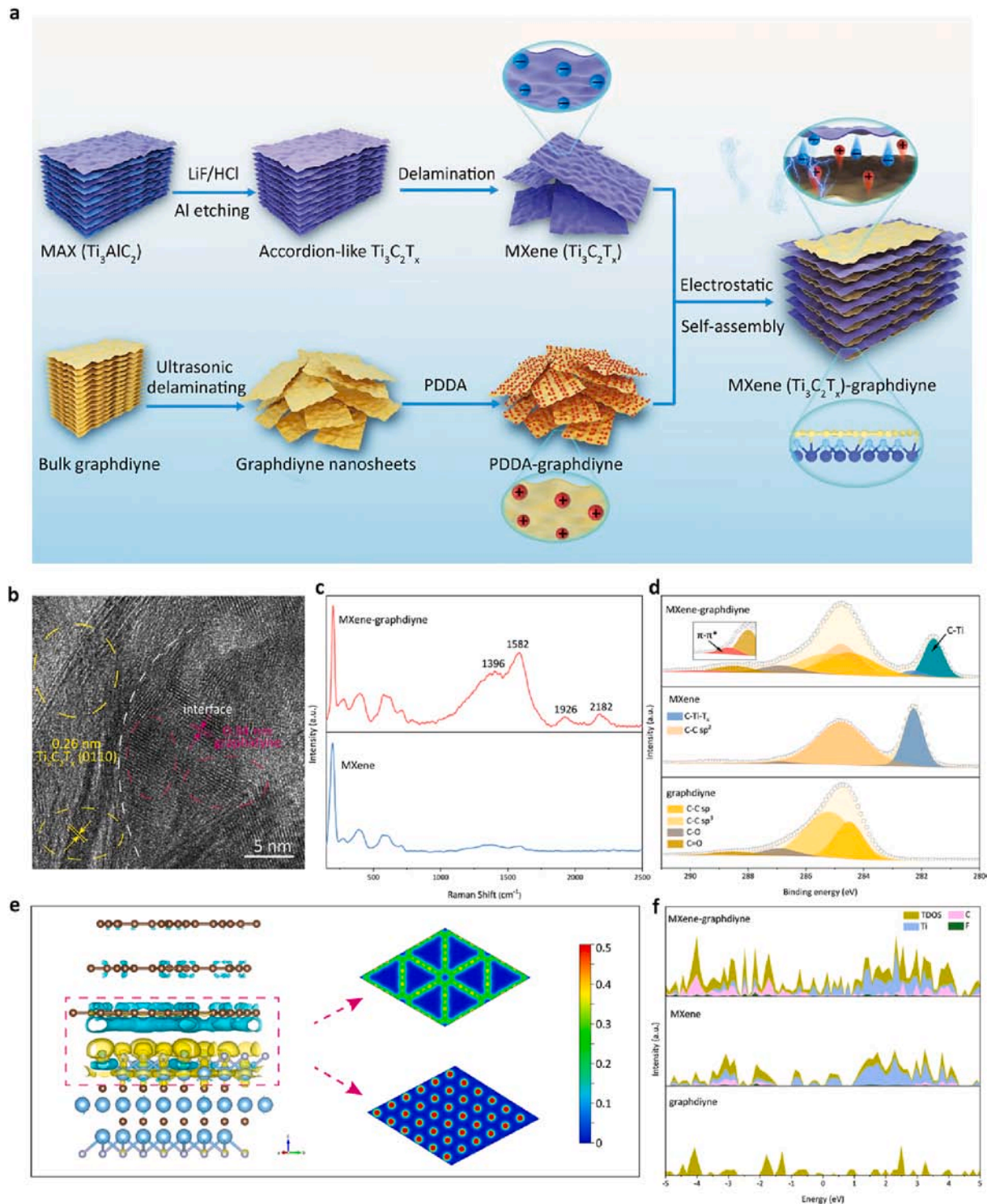


Fig. 2. A) Schematic illustration of the fabrication process for MXene-graphdiyne heterostructure layers. B) HRTEM image of MXene-graphdiyne heterostructure layers. C) Raman spectra of MXene-graphdiyne heterostructure and MXene layers, respectively. D) High resolution of C1s XPS spectra of MXene-graphdiyne heterostructure layers. E) Side and top view of the charge density difference of MXene-graphdiyne. Cyan and yellow areas indicate electron depletion and accumulation, respectively. The electronic local function of MXene-graphdiyne layers indicates the presence of chemical bonding between graphdiyne and MXene at the interface in the MXene-graphdiyne supercell. F) Density of states (DOS) image of MXene-graphdiyne layers, MXene, and graphdiyne, respectively, reflecting MXene-graphdiyne possess a higher density state near the Fermi level compared to MXene and graphdiyne. (For interpretation of the references to colour in this figure legend, the reader is referred to the web version of this article.)

electronic interaction between graphdiyne and MXene layers in MXene-graphdiyne, DFT calculations were performed. Difference charge density analysis (Fig. 2e) demonstrates that graphdiyne forms a chemical bond with MXene through electronic interaction, resulting in electronic

transfer from MXene to graphdiyne at the interface. Moreover, the electronic local function plotted in Fig. 2e confirms the presence of chemical bonding between graphdiyne and MXene at the interface in the MXene-graphdiyne supercell. These interface-induced chemical bonds

promote charge redistribution, resulting in a higher density state near the Fermi level for MXene-graphdiyne compared to MXene and graphdiyne (Fig. 2f) [30,35,36].

To further investigate the surface charge of the MXene-graphdiyne in solution, zeta potential tests were conducted to confirm the charge state in organic electrolyte of lithium-ion batteries. Fig. 3a indicates that

MXene-graphdiyne has a more negative zeta-potential (-90 mV) than those of MXene (-69 mV) and graphdiyne (-57 mV), suggesting a strongly stable interfacial electric double layer can be formed on the surface of MXene-graphdiyne. This negatively charged surface of MXene-graphdiyne promotes substantial positively charged Li ions, thereby accelerating the lithium ion transfer at the interface of electrode

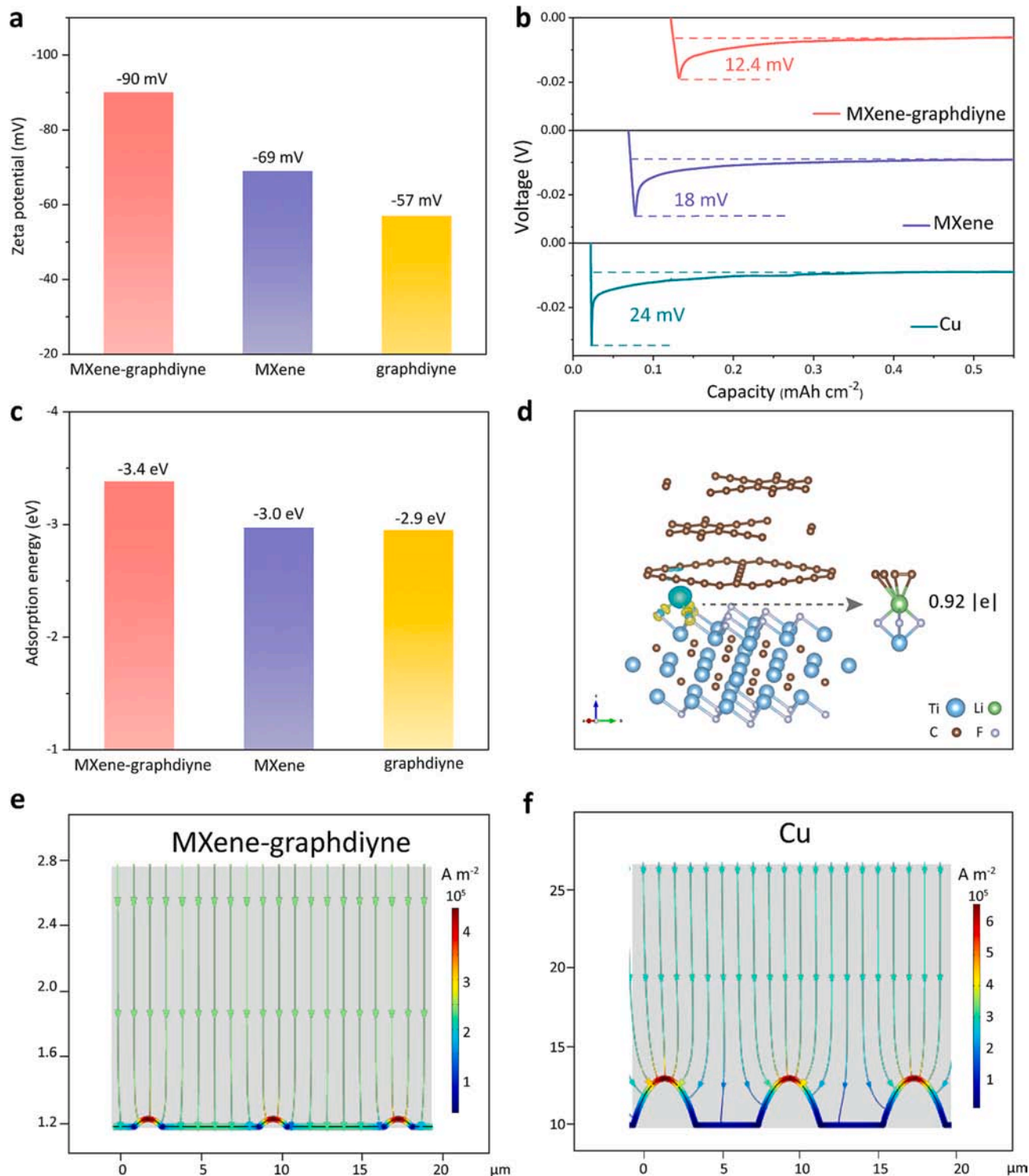


Fig. 3. A) Zeta-potential of MXene-graphdiyne layers, MXene layers, and graphdiyne nanosheets in 1 M LiTFSI in DOL/DME (1:1 vol) with 1.0% LiNO₃, respectively. b) Li nucleation overpotential curves on MXene-graphdiyne layers, MXene layers, and Cu foil, respectively. c) The calculated adsorption energies of a Li atom on the MXene-graphdiyne layers, MXene layers, and graphdiyne nanosheets. d) The deformation charge density of a Li atom absorbed on MXene-graphdiyne heterostructure layers. COMSOL Multiphysics simulations of the electric field distribution in the e) MXene-graphdiyne and f) Cu foil anodes at the initial Li deposition process.

and electrolyte as well as facilitating the homogeneous Li nucleation. Therefore, to investigate the lithium nucleation behaviors on MXene-graphdiyne layers, the overpotential curves of lithium deposition on MXene-graphdiyne layers at the early stage was tested by chronopotentiometry measurement at 0.05 mA cm^{-2} . As expected, MXene-graphdiyne layers delivered a significantly lower overpotential of $\sim 12.4 \text{ mV}$ compared to MXene layers (18 mV), graphdiyne nanosheets (29 mV) (Figure S8) and Cu foils ($24 \sim 26 \text{ mV}$) [32] (Fig. 3b). To further study the low barrier of Li nucleation on MXene-graphdiyne layers, we conducted DFT calculations. As shown in Fig. 3c, MXene-graphdiyne exhibits a lower Li adsorption energy than those of MXene and graphdiyne, demonstrating that the adsorption of Li atoms has been enhanced in the MXene-graphdiyne compared with the individual components. Bader charge analysis (Fig. 3d) reveals that the absorbed lithium atoms severe as an electron donor, with approximately $0.92 |e|$ transferred to the heterostructure interface of MXene-graphdiyne. This results in the MXene-graphdiyne favorably capturing Li and guiding uniform Li deposition at the nucleation stage. Besides, contact angle tests

(Figure S9) also demonstrate that MXene-graphdiyne layers have a relatively small contact angle with electrolyte, which is consistent with the crystal nucleation theory. According to the theory, a small contact angle benefits a low barrier of nucleation, which is in line with the overpotential results discussed earlier.

As for the growth stage of Li deposition, we initially adopted an *in-situ* optical microscope to observe the process of Li deposition on MXene-graphdiyne. MXene-graphdiyne (Figure S10) demonstrate a uniform Li deposition morphology rather than dendrites. Besides, SEM images of MXene-graphdiyne after deposition various Li capacities from 1 to 8 mAh cm^{-2} demonstrated a uniform lithium deposition morphology without dendrites (Figure S11). However, Cu foil exhibited a coarse surface with drastic Li dendrites (Figure S12-S13). To gain a deeper insight into the lithium growth process on MXene-graphdiyne electrode, we established a simulation model of Li deposition using COMSOL Multiphysics based on the roughness of electrode surface (Figure S14). As exhibited in Fig. 3e, the simulation results indicate that the MXene-graphdiyne layers can uniformize the electric field as well as Li^+ flux,

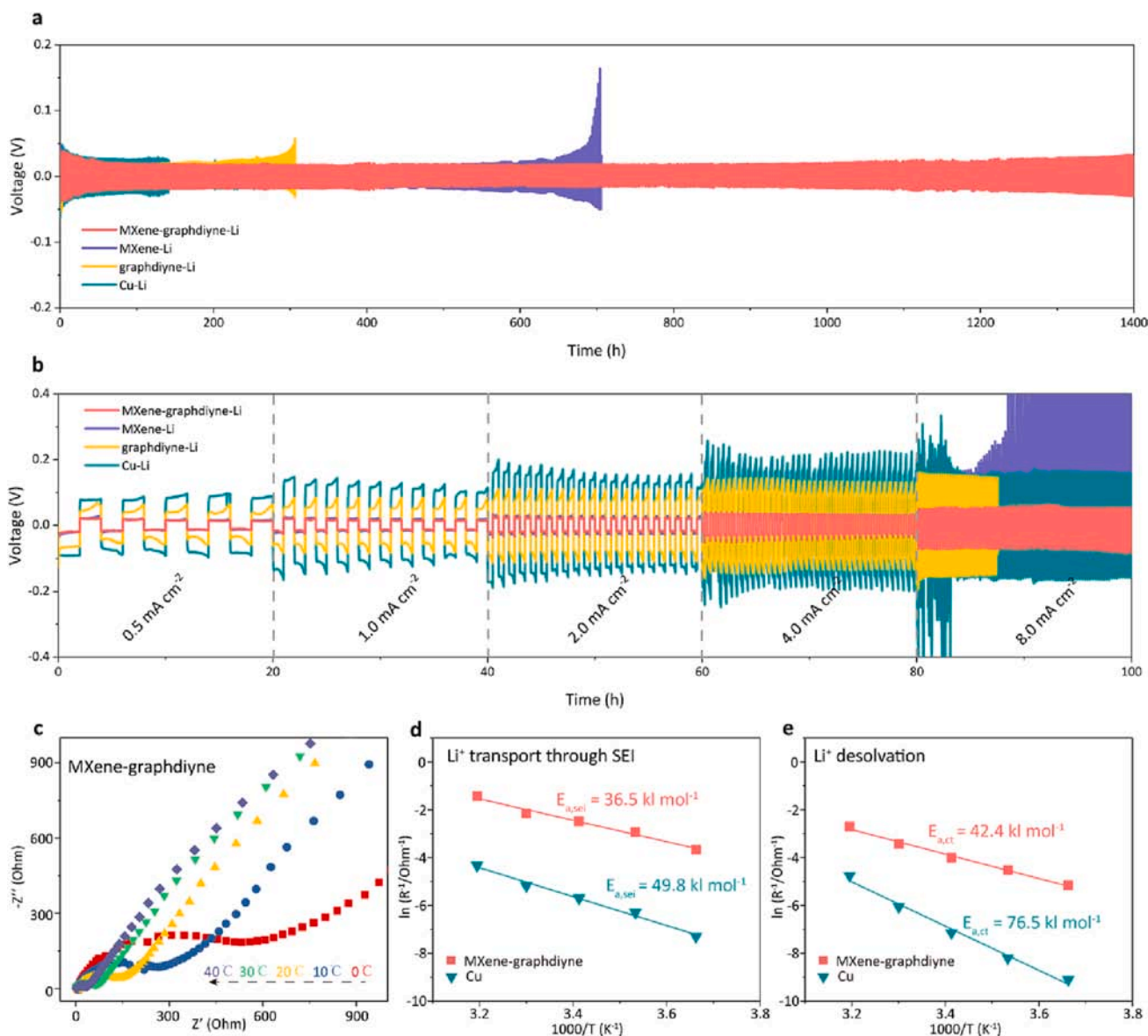


Fig. 4. A) Cyclic properties for symmetric cells with MXene-graphdiyne-Li, MXene-Li, graphdiyne-Li, and Cu-Li anodes at 1.0 mA cm^{-2} and 1.0 mAh cm^{-2} , respectively. b) Rate performances for symmetric cells of MXene-graphdiyne-Li, MXene-Li, graphdiyne-Li, and Cu-Li anodes with various current densities from 0.5 to 8 mA cm^{-2} . c) EIS spectra of MXene-graphdiyne-Li at various temperature from 0 to $40 \text{ }^\circ\text{C}$. Activation energies (E_a) of the reaction for d) SEI and e) charge transfer in MXene-graphdiyne and Cu foil surface, respectively.

thereby facilitating the uniform lithium deposition. In contrast, the Cu electrode (Fig. 3f) with a higher overpotential and uneven surface is more prone to the lightning-rod effect [1] and non-uniform deposition, which can lead to Li dendrite growth.

To systematically assess the electrochemical performance of MXene-graphdiyne layers, MXene layers, graphdiyne nanosheets, and Cu foil, lithium anodes were fabricated by electrochemically depositing metallic Li. The cycling performance of the resulting MXene-graphdiyne-Li,

MXene-Li, graphdiyne-Li, and Cu-Li anodes was then tested by galvanostatic discharge-charge in symmetric cells. MXene-graphdiyne-Li (Fig. 4a) demonstrated an ultralong cycle life of more than 1400 h, which was superior to those of MXene-Li (~700 h), graphdiyne-Li (~300 h), and Cu-Li (~200 h) tested under the same conditions (1 mA cm^{-2} and 1 mAh cm^{-2}). Furthermore, a low mass-controlled voltage polarization of MXene-graphdiyne-Li anode remained less than 30 mV even after cycling for 1400 h, indicating fast transfer of lithium ions and

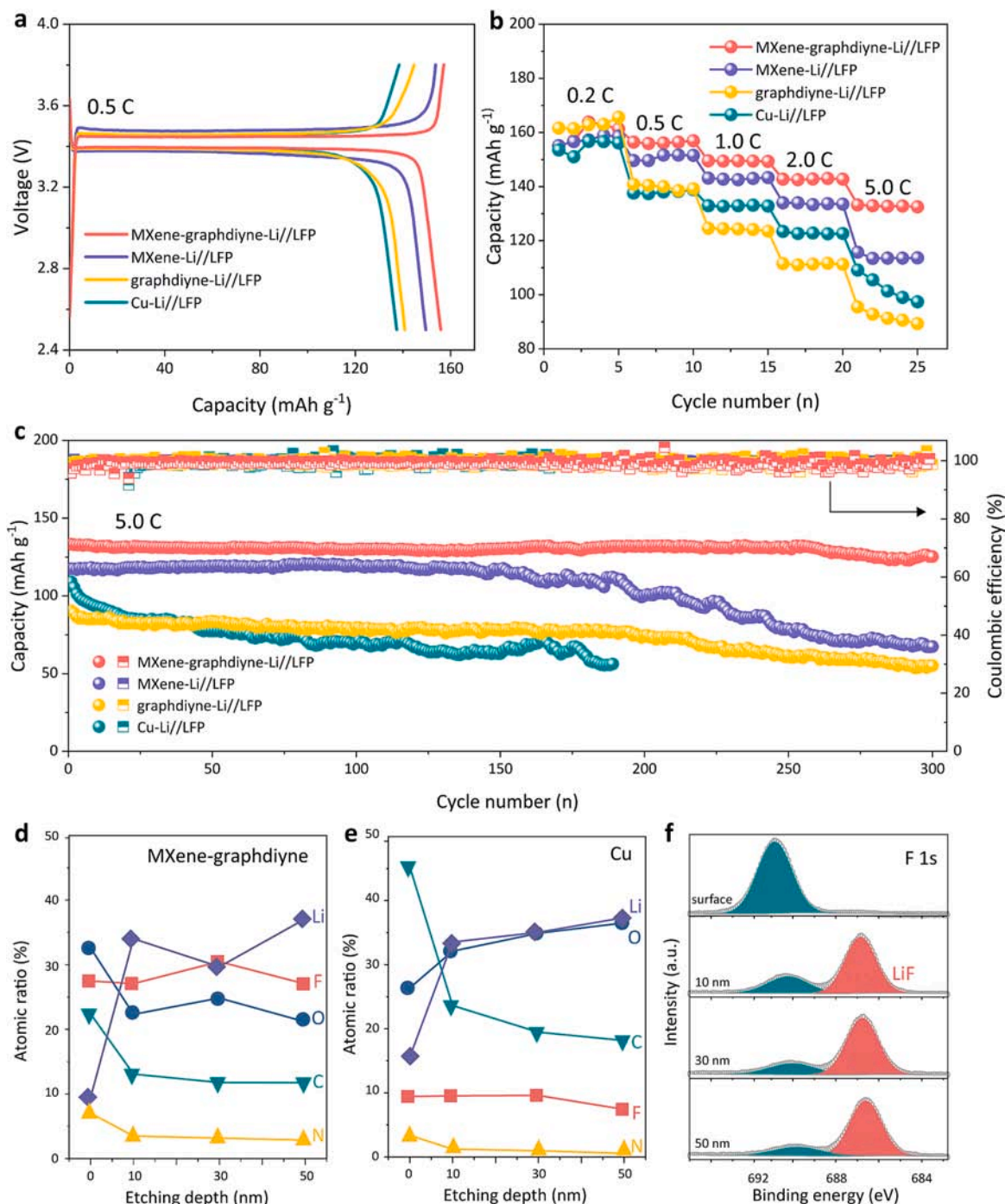


Fig. 5. a) Charge-discharge voltage profiles of MXene-graphdiyne-Li//LFP, MXene-Li//LFP, graphdiyne-Li//LFP, and Cu-Li//LFP full cells at 0.5C. b) Rate performances of MXene-graphdiyne-Li//LFP, MXene-Li//LFP, graphdiyne-Li//LFP, and Cu-Li//LFP at the various rate from 0.2 to 5.0C. c) Cyclic performance and Coulombic efficiency of MXene-graphdiyne-Li//LFP, MXene-Li//LFP, graphdiyne-Li//LFP, and Cu-Li//LFP full cells at 5.0C. d) The elemental composition of Li, F, O, C, and N from the surface to a depth (~50 nm) in MXene-graphdiyne-Li by XPS depth profiling, indicating an increase in F content to nearly 28% across the entire anode surface. e) The elemental composition of Li, F, O, C, and N from the surface to a depth (~50 nm) in Cu-Li by XPS depth profiling. f) High resolution XPS of F1s, demonstrating a significant portion of the F is present in the form of LiF, accounting for approximately 81% of the SEI layers.

electrons. Rate capabilities of the anodes were evaluated at various current densities ranging from 0.5 to 8 mA cm⁻². MXene-graphdiyne-Li anode exhibited a high rate capability (8 mA cm⁻²) with a low overpotential (~50 mV) (Fig. 4b and Figure S15), superior to those of MXene-Li (~150 mV), graphdiyne-Li (~150 mV) and Cu-Li (~200 mV) anodes, as well as the reported Li-based anodes (80–200 mV) [28,38]. These superior electrochemical performances of MXene-graphdiyne-Li anode can be attributed to its high zeta-potential, which facilitates the interface charge transfer. To verify this viewpoint, we prepared a compound of MXene and graphdiyne using a liquid phase stirring method. The resulting compound demonstrated a zeta-potential of approximately -61 mV (Figure S16). However, when used in Li composite anodes, it exhibited a high nucleation overpotential of around 21 mV (Figure S17), poor cyclic performance (~600 h) (Figure S18), and low rate capabilities (Figure S19) compared to that of MXene-graphdiyne layers. This indicates that a high-zeta-potential is crucial for promoting Li deposition and enhancing the electrochemical property of metallic anodes. Besides, high capacity of 5 mAh cm⁻² has been adopted to test the deep stripping-plating property of MXene-graphdiyne-Li anode. As shown in Figure S20, MXene-graphdiyne-Li anode exhibits a cycle life up to 500 h, indicating the potential practical application. Furthermore, we observed the overall morphology and structural integrity of the MXene-graphdiyne anode after being cycled by analyzing the SEM images (Figure S21).

To further investigate the influence of interface charge transfer on the electrochemical performance, electrochemical impedance spectroscopy (EIS) was performed to analyze the interface kinetics. As exhibited in Fig. 4c, S22 and Table S1, the MXene-graphdiyne-Li anode exhibited a low charge transfer resistance of ~31 Ω at 30 °C, which is superior to that of Cu-Li (~430 Ω). Besides, activation energies of lithium ion transport through SEI ($E_{a,SEI}$) and charge transfer ($E_{a,ct}$) of MXene-graphdiyne anodes were calculated using the temperature-dependent EIS spectra fitted by Arrhenius law. The energy barrier for Li⁺ transportation in MXene-graphdiyne (Fig. 4d) was found to be lower (36.5 kJ mol⁻¹) than that of Cu foil (46.8 kJ mol⁻¹) and the reported Li-based anodes [39], suggesting that MXene-graphdiyne can form a stable SEI layer with a low energy barrier, facilitating Li⁺ transportation. Furthermore, the $E_{a,ct}$ of MXene-graphdiyne (42.4 kJ mol⁻¹) was found to be significantly lower than that of Cu foil (76.8 kJ mol⁻¹) (Fig. 4e), which is generally considered the dominant barrier in the electrochemical process [40]. The kinetics analysis suggests that the high-zeta-potential interphase derived from MXene-graphdiyne enable the fast transfer of Li⁺ and electrons in lithium metal batteries.

Therefore, full cells comprising MXene-graphdiyne-Li anode and LiFeO₄ cathode were investigated by galvanostatic discharge-charge at various rates. MXene-graphdiyne-Li-LiFeO₄ full cell delivered a high reversible specific capacity of 160 mAh g⁻¹ at 0.5C, superior to those of MXene-Li//LiFeO₄ (150 mAh g⁻¹), graphdiyne-Li//LiFeO₄ (141 mAh g⁻¹) and Cu-Li//LiFeO₄ (138 mAh g⁻¹) (Fig. 5a). Additionally, MXene-graphdiyne-Li//LiFeO₄ full cell exhibits much better rate capabilities (Fig. 5b) due to the fast transfer of Li⁺ as well as electrons. When subjected to a high rate of 5.0C (Fig. 5c), MXene-graphdiyne-Li//LiFeO₄ full cell represents a good reversible specific capacity of 130 mAh g⁻¹ and stable Coulombic efficiency (~99%) after 300 cycles, outperforming MXene-Li//LiFeO₄ (75 mAh g⁻¹), graphdiyne-Li//LiFeO₄ (60 mAh g⁻¹), and Cu-Li//LiFeO₄ (64 mAh g⁻¹ at 170th cycles) full cells. These demonstrate that MXene-graphdiyne-Li//LiFeO₄ full cell possesses superior cycling stability compared to MXene-Li//LiFeO₄ and Cu-Li//LiFeO₄ full cells. To further investigate the good electrochemical performance obtained by MXene-graphdiyne//Li anodes, XPS measurements were performed (Figure S23). As shown in Fig. 5d, XPS depth profiling from the surface to 50 nm indicates an increase in F content to nearly 28% across the entire anode surface. In contrast, Cu anodes show a very low F content of less than 10%. High-resolution XPS spectra of F (Fig. 5e) demonstrate that most of the F belongs to LiF, accounting for about 81% of the SEI layers. This LiF content can greatly accelerate the

fast transfer of Li⁺ and electrons, thereby contributing to the excellent electrochemical performance of MXene-graphdiyne-Li//LiFeO₄ full cells.

3. Conclusions

We have successfully fabricated MXene-graphdiyne heterostructure layers with high-zeta-potential by a facile method of electrostatic self-assembly. The high-zeta-potential enables the uniform Li nucleation on MXene-graphdiyne heterojunction layers by accelerating the interface charge transfer. COMSOL Multiphysics simulations further reveal the MXene-graphdiyne can highly reduce the lithium ion concentration gradient and homogenize the electric field in the anodes. As a result, a low overpotential of 12.4 mV has been exhibited by MXene-graphdiyne layers at 0.05 mA cm⁻². Besides, MXene-graphdiyne-Li anodes display an ultralong cycle life upto 1400 h and good rate capability upto 8 mA cm⁻². Moreover, when combined with LiFeO₄ cathodes, the full cells maintained stable cycling properties for 300 cycles at 5C. We believe that this approach utilizing a high zeta-potential can be extended to other metal anodes, resulting in dendrite-free anodes with excellent performance.

4. Experimental section

4.1. Preparation of graphdiyne nanosheets

Graphdiyne nanosheets were exfoliated from the bulk graphdiyne using the previously reported methods. The few-layer graphdiyne flakes were mechanically exfoliated from bulk graphdiyne using a high-power ultrasonic probe with the protection of Ar atmosphere.

4.2. Preparation of MXene-graphdiyne heterostructure layers

The graphdiyne nanosheets were modified with a cationic polymer, poly(diallyldimethylammonium chloride) (PDDA), to provide a surface positive charge. Typically, 5 mg PDDA slowly added into 50 mL graphdiyne suspension (1 mg mL⁻¹) and sonication for 1 h. Then, 50 mL PDDA-modified graphdiyne suspension slowly added into 50 mL MXene (1 mg mL⁻¹) suspension and subsequently ultrasonic for 1 h. In this process, the positively charged graphdiyne nanosheets were electrostatically attached to the negatively charged MXene. After the removal of PDDA, the 2D MXene-graphdiyne layers were obtained by freeze drying (Fig. 2a).

4.3. The preparation of MXene (Ti₃C₂T_x) nanosheets

1 g Ti₃AlC₂ powder was immersed into 20 mL aqueous HCl solutions (5 M) with 3.2 g LiF by stirring for 40 h to etch Al layers. After repeatedly washed by distilled water and subsequent freeze-drying. The as-prepared Ti₃C₂T_x nanosheets were obtained.

Declaration of Competing Interest

The authors declare that they have no known competing financial interests or personal relationships that could have appeared to influence the work reported in this paper.

Data availability

Data will be made available on request.

Acknowledgements

This work is supported partially by project of State Key Laboratory of Alternate Electrical Power System with Renewable Energy Sources (LAPS21004, LAPS202114), National Natural Science Foundation of

China (Grant nos. 52102203, 52272200, 51972110, 52102245 and 52072121), Beijing Science and Technology Project (Z211100004621010), Beijing Natural Science Foundation (2222076, 2222077), Hebei Natural Science Foundation (E2022502022), Huaneng Group Headquarters Science and Technology Project (HNKJ20-H88), 2022 Strategic Research Key Project of Science and Technology Commission of the Ministry of Education, China Postdoctoral Science Foundation (2022 M721129) and the Fundamental Research Funds for the Central Universities (2022MS030, 2021MS028, 2020MS023, 2020MS028) and the NCEPU “Double First-Class” Program. The authors wish to acknowledge Dr. Zhongheng Fu from University of Science and Technology Beijing for his assistance with DFT calculations. The authors also wish to acknowledge Prof. Jun Yan from Harbin Engineering University for his assistance.

Appendix A. Supplementary data

Supplementary data to this article can be found online at <https://doi.org/10.1016/j.cej.2023.144014>.

References

- Z. Wang, H. Jiang, Y. Zhang, Y. An, C. Wei, L. Tan, S. Xiong, Y. Qian, J. Feng, Application of 2D MXene in organic electrode materials for rechargeable batteries: recent progress and perspectives, *Adv. Funct. Mater.* 33 (12) (2023) 2210184.
- W. Liu, P. Liu, D. Mitlin, Review of emerging concepts in SEI analysis and artificial SEI membranes for lithium, sodium, and potassium metal battery anodes, *Adv. Energy Mater.* 10 (43) (2020) 2002297.
- D. Wang, C. Han, F. Mo, Q. Yang, Y. Zhao, Q. Li, G. Liang, B. Dong, C. Zhi, Energy density issues of flexible energy storage devices, *Energy Storage Materials* 28 (2020) 264–292.
- H. Jiang, X. Lin, C. Wei, J. Feng, X. Tian, Scalable synthesis of nano-sized Bi for separator modifying in 5V-class lithium metal batteries and potassium ion batteries anodes, *Small* 18 (4) (2022) 2104264.
- Z. Huang, T. Wang, X. Li, H. Cui, G. Liang, Q.i. Yang, Z.e. Chen, A.o. Chen, Y. Guo, J. Fan, C. Zhi, Small-dipole-molecule-containing electrolytes for high-voltage aqueous rechargeable batteries, *Adv. Mater.* 34 (4) (2022) 2106180.
- J. Gu, Y. Tao, H. Chen, Z. Cao, Y. Zhang, Z. Du, Y. Cui, S. Yang, Stress-release functional liquid metal-MXene layers toward dendrite-free zinc metal anodes, *Adv. Energy Mater.* 12 (16) (2022) 202200115.
- X. Shi, J. Wang, F. Yang, X. Liu, Y. Yu, X. Lu, Metallic zinc anode working at 50 and 50 mAh cm⁻² with high depth of discharge via electrical double layer reconstruction, *Adv. Funct. Mater.* 33 (7) (2023) 202211917.
- Y. An, Y. Tian, C. Liu, S. Xiong, J. Feng, Y. Qian, One-step, vacuum-assisted construction of micrometer-sized nanoporous silicon confined by uniform two-dimensional N-doped carbon toward advanced Li ion and MXene-based Li metal batteries, *ACS Nano* 16 (3) (2022) 4560–4577.
- X. Li, M. Li, K. Luo, Y. Hou, P. Li, Q.i. Yang, Z. Huang, G. Liang, Z.e. Chen, S. Du, Q. Huang, C. Zhi, Lattice matching and halogen regulation for synergistically induced uniform zinc electrodeposition by halogenated Ti₃C₂ MXenes, *ACS Nano* 16 (1) (2022) 813–822.
- R. Luo, B. Xi, R. Wei, W. Chen, X. Ma, Z. Feng, J. Feng, S. Xiong, N-doped graphitic ladder-structured carbon nanotubes as a superior sulfur host for lithium–sulfur batteries, *Inorg. Chem. Front.* 7 (20) (2020) 3969–3979.
- Y. An, Y. Tian, Y. Zhang, C. Wei, L. Tan, C. Zhang, N. Cui, S. Xiong, J. Feng, Y. Qian, Two-dimensional silicon/carbon from commercial alloy and CO₂ for lithium storage and flexible Ti₃C₂T_x MXene-based lithium-metal batteries, *ACS Nano* 14 (12) (2020) 17574–17588.
- N. Shi, B. Xi, Z. Feng, J. Liu, D. Wei, J. Liu, J. Feng, S. Xiong, Strongly coupled W₂C atomic nanoclusters on N/P-codoped graphene for kinetically enhanced sulfur host, *Adv. Mater. Interfaces* 6 (9) (2019) 1802088.
- J. Gu, H. Chen, Y. Shi, Z. Cao, Z. Du, B. Li, S. Yang, Eliminating lightning-rod effect of lithium anodes via sine-wave analogous MXene layers, *Adv. Energy Mater.* 12 (36) (2022) 2201181, <https://doi.org/10.1002/aenm.202201181>.
- P. Zhai, L. Liu, X. Gu, T. Wang, Y. Gong, Interface engineering for lithium metal anodes in liquid electrolyte, *Adv. Energy Mater.* 10 (34) (2020) 2001257.
- M.D. Tikekar, S. Choudhury, Z. Tu, L.A. Archer, Design principles for electrolytes and interfaces for stable lithium-metal batteries, *Nature Energy* 1 (9) (2016) 1–7.
- W. Xu, J. Wang, F. Ding, X. Chen, E. Nasybulin, Y. Zhang, J.-G. Zhang, Lithium metal anodes for rechargeable batteries, *Energy Environ. Sci.* 7 (2) (2014) 513–537.
- Q.i. Yang, Y. Guo, B. Yan, C. Wang, Z. Liu, Z. Huang, Y. Wang, Y. Li, H. Li, L.i. Song, J. Fan, C. Zhi, Hydrogen-substituted graphdiyne ion tunnels directing concentration redistribution for commercial-grade dendrite-free zinc anodes, *Adv. Mater.* 32 (25) (2020) 2001755.
- Z. Hao, Y. Zhang, Z. Hao, G. Li, Y. Lu, S. Jin, G. Yang, S. Zhang, Z. Yan, Q. Zhao, J. Chen, Metal anodes with ultrahigh reversibility enabled by the closest packing crystallography for sustainable batteries, *Adv. Mater.* 35 (9) (2023) 202209985.
- J. Bai, B. Xi, H. Mao, Y. Lin, X. Ma, J. Feng, S. Xiong, One-step construction of N, P-codoped porous carbon sheets/CoP hybrids with enhanced lithium and potassium storage, *Adv. Mater.* 30 (35) (2018) 1802310.
- K. Su, T. Jin, C.H. Zhang, S. Yuan, N.W. Li, L. Yu, Quasi-metallic lithium encapsulated in the subnanopores of hard carbon for hybrid lithium-ion/lithium metal batteries, *Chem. Eng. J.* 450 (2022), 138049.
- X. Cao, X. Ren, L. Zou, M.H. Engelhard, W. Huang, H. Wang, B.E. Matthews, H. Lee, C. Niu, B.W. Arey, Y.i. Cui, C. Wang, J. Xiao, J. Liu, W.u. Xu, J.-G. Zhang, Monolithic solid–electrolyte interphases formed in fluorinated orthoformate-based electrolytes minimize Li depletion and pulverization, *Nature Energy* 4 (9) (2019) 796–805.
- X. Zhang, Y. Chen, F. Ma, X. Chen, B. Wang, Q. Wu, Z. Zhang, D. Liu, W. Zhang, J. He, Z.-L. Xu, Regulating Li uniform deposition by lithiophilic interlayer as Li-ion redistributor for highly stable lithium metal batteries, *Chem. Eng. J.* 436 (2022), 134945.
- T. Jin, M. Liu, K. Su, Y. Lu, G. Cheng, Y. Liu, N.W. Li, L. Yu, Polymer zwitterion-based artificial interphase layers for stable lithium metal anodes, *ACS Appl. Mater. Interfaces* 13 (48) (2021) 57489–57496.
- R. Zhang, X.-R. Chen, X. Chen, X.-B. Cheng, X.-Q. Zhang, C. Yan, Q. Zhang, Lithiophilic sites in doped graphene guide uniform lithium nucleation for dendrite-free lithium metal anodes, *Angew. Chem. Int. Ed.* 129 (27) (2017) 7872–7876.
- X. Qian, X. Fan, Y. Peng, P. Xue, C. Sun, X. Shi, C. Lai, J. Liang, Polysiloxane cross-linked mechanically stable MXene-based lithium host for ultrastable lithium metal anodes with ultrahigh current densities and capacities, *Adv. Funct. Mater.* 31 (6) (2021) 2008044.
- Y. Yuan, F. Wu, Y. Bai, Y. Li, G. Chen, Z. Wang, C. Wu, Regulating Li deposition by constructing LiF-rich host for dendrite-free lithium metal anode, *Energy Storage Mater.* 16 (2019) 411–418.
- J. Liu, M. Wu, X. Li, D. Wu, H. Wang, J. Huang, J. Ma, Amide-functional, Li₃N, LiF-rich heterostructured electrode electrolyte interphases for 4.6 V Li||LiCoO₂ batteries, *Adv. Energy Mater.* (2023) 2300084.
- P. Qing, Z. Wu, A. Wang, S. Huang, K. Long, T. Naren, D. Chen, P. He, H. Huang, Y. Chen, L. Mei, L. Chen, Highly reversible lithium metal anode enabled by 3D lithiophilic-lithiophobic dual-skeletons, *Adv. Mater.* (2023) 2211203.
- S. Jin, Y. Ye, Y. Niu, Y. Xu, H. Jin, J. Wang, Z. Sun, A. Cao, X. Wu, Y.i. Luo, H. Ji, L.-J. Wan, Solid–solution-based metal alloy phase for highly reversible lithium metal anode, *J. Am. Chem. Soc.* 142 (19) (2020) 8818–8826.
- J. Yan, C.E. Ren, K. Maleski, C.B. Hatter, B. Anasori, P. Urbankowski, A. Sarycheva, Y. Gogotsi, Flexible MXene/graphene films for ultrafast supercapacitors with outstanding volumetric capacitance, *Adv. Funct. Mater.* 27 (30) (2017) 1701264.
- J. Li, T. Jiu, S. Chen, L.e. Liu, Q. Yao, F. Bi, C. Zhao, Z. Wang, M. Zhao, G. Zhang, Y. Xue, F. Lu, Y. Li, Graphdiyne as a host active material for perovskite solar cell application, *Nano Lett.* 18 (11) (2018) 6941–6947.
- F. Xu, K. Meng, B. Zhu, H. Liu, J. Xu, J. Yu, Graphdiyne: a new photocatalytic CO₂ reduction cocatalyst, *Adv. Funct. Mater.* 29 (43) (2019) 1904256.
- Y. Fang, Y. Xue, L. Hui, H. Yu, Y. Li, Graphdiyne@Janus magnetite for photocatalytic nitrogen fixation, *Angew. Chem. Int. Ed.* 133 (6) (2021) 3207–3211.
- L. Jiao, C. Zhang, C. Geng, S. Wu, H. Li, W. Lv, Y. Tao, Z. Chen, G. Zhou, J. Li, G. Ling, Y. Wan, Q.-H. Yang, Capture and catalytic conversion of polysulfides by in situ built TiO₂-MXene heterostructures for lithium–sulfur batteries, *Adv. Energy Mater.* 9 (19) (2019) 1900219.
- G. Li, Y. Li, H. Liu, Y. Guo, Y. Li, D. Zhu, Architecture of graphdiyne nanoscale films, *Chem. Commun.* 46 (19) (2010) 3256–3258.
- Y. Fang, Y. Xue, Y. Li, H. Yu, L. Hui, Y. Liu, C. Xing, C. Zhang, D. Zhang, Z. Wang, Graphdiyne interface engineering: highly active and selective ammonia synthesis, *Angew. Chem. Int. Ed.* 59 (31) (2020) 13021–13027.
- H. Yu, Y. Xue, L. Hui, C. Zhang, Y. Zhao, Z. Li, Y. Li, Controlled growth of MoS₂ nanosheets on 2D N-doped graphdiyne nanolayers for highly associated effects on water reduction, *Adv. Funct. Mater.* 28 (19) (2018) 1707564.
- Y. Guo, P. Niu, Y. Liu, Y. Ouyang, D. Li, T. Zhai, H. Li, Y. Cui, An autotransferable g-C₃N₄ Li⁺-modulating layer toward stable lithium anodes, *Adv. Mater.* 31 (27) (2019) 1900342.
- C. Yan, H.-R. Li, X. Chen, X.-Q. Zhang, X.-B. Cheng, R. Xu, J.-Q. Huang, Q. Zhang, Regulating the inner Helmholtz plane for stable solid electrolyte interphase on lithium metal anodes, *J. Am. Chem. Soc.* 141 (23) (2019) 9422–9429.
- K. Xu, A. von Cresce, U. Lee, Differentiating contributions to “ion transfer” barrier from interphasial resistance and Li⁺ desolvation at electrolyte/graphite interface, *Langmuir* 26 (13) (2010) 11538–11543.